OPTICA

Ultralow voltage, high-speed, and energy-efficient cryogenic electro-optic modulator

PAOLO PINTUS,[1,2,5,†] ANSHUMAN SINGH,[3,†] WEIQIANG XIE,[1,†] LEONARDO RANZANI,[3] MARTIN V. GUSTAFSSON,[3] MINH A. TRAN,[1,4] CHAO XIANG,[1] JONATHAN PETERS,[1] JOHN E. BOWERS,[1] AND MOE SOLTANI[3,*]

[1] Department of Electrical and Computer Engineering, University of California, Santa Barbara, California 93106, USA
[2] Department of Physics, University of Cagliari, Monserrato 09042, Italy
[3] Raytheon BBN Technologies, 10 Moulton Street, Cambridge, Massachusetts 02138, USA
[4] Currently with Nexus Photonics, Goleta, California 93117, USA
[5] e-mail: ppintus@ece.ucsb.edu
*Corresponding author: mo.soltani@raytheon.com

Received 11 May 2022; revised 17 August 2022; accepted 20 September 2022; published 20 October 2022

Photonic integrated circuits (PICs) at cryogenic temperatures enable a wide range of applications in scalable classical and quantum systems for computing and sensing. A promising application of cryogenic PICs is to provide optical interconnects by upconverting signals from the electrical to the optical domain, allowing a massive data transfer from 4 K superconducting (SC) electronics to the room temperature environment. Such a solution can overcome a major bottleneck in the scalability of cryogenic systems that currently rely on bulky coaxial cables that suffer from limited bandwidth, a large heat load, and poor scalability. A key element to realize a cryogenic-to-room temperature optical interconnect is a high-speed, electro-optic (EO) modulator operating at 4 K with a modulation voltage at the mV scale, compatible with SC electronics. Although several cryogenic EO modulators have been demonstrated, their driving voltages are substantially large (several hundred mV to a few V) compared to the mV scale voltage provided by SC circuits. Here, we demonstrate a cryogenic modulator with ∼10 mV peak-to-peak driving voltage and Gb/s data rate, with an ultralow electric energy consumption of ∼10.4 aJ/bit and an optical energy consumption of ∼213 fJ/bit. We achieve this record performance by designing and fabricating a compact optical ring resonator modulator in a heterogeneous InP-on-Si platform, where we optimize a multi-quantum-well layer of InAlGaAs to achieve a strong EO effect at 4 K. Unlike other semiconductors such as silicon, our platform benefits from the high-carrier mobility and minimal free-carrier freezing of III-V compounds at low temperatures, with a moderate doping level and a correspondingly low loss (intrinsic resonator $Q \sim 272{,}000$). These modulators can pave the path for complex cryogenic photonic functionalities and massive data transmission between cryogenic and room-temperature electronics. © 2022 Optica Publishing Group under the terms of the Optica Open Access Publishing Agreement

https://doi.org/10.1364/OPTICA.463722

1. INTRODUCTION

A class of next generation classical and quantum computing systems [1–4] and sensors [5,6] will operate at cryogenic temperatures (∼4 K) based on superconducting and optical technologies. A major challenge in these platforms is providing high-speed, energy efficient transfer of massive amounts of data (e.g., hundreds of Gb/s to Tb/s) to room temperature. Commonly used coaxial cables have limited communications bandwidth, a large propagation loss, and add an excessive heat load to the cryogenic stage [3,4]. Thus, they will not be a scalable solution for the data transmission from cold to room temperature, as the heat load counteracts the energy efficiency gained by using superconducting and other low-temperature circuits, and can easily exceed the cooling power of available cryocoolers as systems scale.

The stringent cooling power requirement of cryogenic systems is another constraint that demands a data interconnect link with minimal energy consumption at low-temperatures. In concrete terms, each watt of power dissipated at 4 K temperature translates to roughly several hundred watts of power dissipated at room temperature in practical lab-scale cooling equipment [7]. Therefore, it is highly desirable to implement a scalable data interconnect link between 4 K and room temperature, with majority of the energy consumption imparted on the room temperature components of the link.

To overcome these limitations, a promising solution is to use integrated electro-optic (EO) modulators in a photonic integrated circuit (PIC) platform at a temperature of 4 K to upconvert/multiplex data from the electrical to the optical domain and transmit them to room temperature via optical fibers [3,8,9]. This approach has two main advantages: (i) it provides wide data

bandwidth with a potential aggregate data capacity of tens of Tb/s to Pb/s, extremely low loss, and negligible heat transfer; and (ii) it allows substantial reduction of interconnect energy consumption inside the cryocooler, and imparts the majority of the energy consumption on the room temperature components of the link (e.g., room temperature amplifiers).

To achieve this goal, the modulator must operate efficiently at a temperature of ~4 K and respond to high-speed, low-voltage digital signals, typically on the scale of millivolts [1,5,10–12]. There have been several recent demonstrations of cryogenic EO modulators based on different material platforms [8,13–18]. However, these EO platforms operate at modulation voltages 2–3 orders of magnitude higher than the typical voltages provided by SC circuits (< ~10 mV). In addition, not all EO platforms can operate reliably at low temperatures. Common EO materials such as polymers and lithium niobate are prone to photorefractive instability at low temperatures, making them ill-suited to interface with SC circuitry [19,20]. Long-established silicon (Si) EO modulators based on free-carrier plasma dispersion become inefficient below a few tens of kelvin due to free carrier freeze-out [21]. Although this effect can be compensated to some degree by increasing the doping concentration in the Si, it does not improve the voltage sensitivity of the modulator [8,15]. It also does not address the increased insertion loss due to excess free carriers. A recent promising publication about cryogenic Si modulators uses a monolithically integrated cryogenic voltage amplifier before the modulator to provide the large modulation voltage required for the modulator, but at the cost of substantially increasing the total energy consumption due to dissipation in the cryogenic amplifier [16]. Si modulators based on the DC–Kerr induced Pockels effect have been demonstrated at 4 K; however, the required modulation signal is on the scale of volts [17]. Plasmonic slotted waveguide modulators filled with EO polymer have been demonstrated at room temperature with high speed and low electrical energy consumption (<100 aJ/bit), but they operate at several hundred millivolts of modulation and suffer from a large optical material loss as well as a large coupling loss due to mode mismatch between the straight ridge waveguide region and the slotted waveguide [22,23]. Additionally, the material stability of EO polymers at a 4 K temperature is not well known and susceptible to degradation over time. 2D material-based modulators [22] have been investigated at 4 K, but the modulation voltage is still more than two orders of magnitude higher than what is required to interface with SC circuitry [18].

Here, we demonstrate a cryogenic InP-on-Si photonic (CRISP) ring modulator (Fig. 1) which achieves a Gb/s data rate with a low modulation voltage (10 mV_{pp}). The electrical and optical energy consumption is 10.4 aJ/bit and 213 fJ/bit, respectively, at a temperature of 4 K. The CRISP modulator is fabricated in a heterogeneous platform that combines the strong EO properties of InP—and its associated III-V alloys—with scalable and compact Si photonic circuitry [24–27]. Unlike all-Si modulators, the CRISP modulator suffers minimally from free carrier freezing at low temperatures. This allows it to operate efficiently with moderate doping levels in the InP layer, thus enabling high Q resonators. We design the modulators for operation at 4 K and a wavelength range within 1500–1600 nm. Since the interconnect link is short distance (e.g., <10-meter fiber), there is less restriction on the operation optical wavelength. The demonstrated results in this work are for L-band (~1600 nm wavelength).

2. DEVICE DESIGN AND FABRICATION

A schematic of the CRISP modulator is shown in Fig. 1(a), where the stack of III-V compounds sits on a Si ring, which is evanescently coupled to a Si rib waveguide. The III-V region is a P-N junction diode with the QW heterostructure sandwiched in it. Two strong modulation mechanisms are present in the III-V compounds used in the modulator: band-filling (Burstein–Moss) [28] and quantum-confined Stark effects (QCSE) [29,30] , with some additional contributions from plasma dispersion [28]. We design a multi-quantum well (QW) layer to enhance the EO effects, which leads to a large modulation. To further increase the modulation sensitivity to millivolt-scale voltages, we take advantage of a ring resonator configuration with a sharp resonance spectrum. This enables intensity modulation of the light with modulation voltages as small as ~10 mV_{pp} and even lower.

Part of the III-V heterostructure is grown as a multi-quantum well (QW), and this structure is essential to achieve high-sensitivity modulation at 4 K. The doping of the QW layer is optimized to achieve large band-filling and plasma effects with negligible optical absorption, while the III-V composition and the geometry of the QWs are engineered to maximize the QCSE. Specifically, the QCSE is caused by the interaction of light with exciton quasiparticles (electron-hole bound states) and becomes much stronger at lower temperatures due to the sharper exciton spectrum [29].

A simplified cross-section of the InP-on-Si modulator is shown in Fig. 1(b), where the EO layer consists of a stack of 15 alternate QWs and quantum barriers (QBs). Each QW has a thickness of 8 nm and is sandwiched between 5 nm thick QBs. This multi-QW/QB layer is also inserted between two 125 nm thick separate confinement heterostructures (SCHs) that confine electrons and holes in the EO layer. This design allows for a large overlap between electron and hole wave functions [inset in Fig. 1(c)], which maximizes the QCSE effect. The QWs, QBs, and SCHs are made of In_xAl_{1-x-y} Ga_yAs, which provides a large bandgap offsetuseful for energy band engineering [31]and higher fabrication yield than $In_{1-x}Ga_xAs_{1-y}P_y$.

We optimize the dimensions of the Si and the InP layer for maximum optical modal overlap, as shown in Fig. 1(d). For this purpose, we chose a Si layer with a thickness of 500 nm and etched it down to 260 nm to produce a rib-type waveguide optical index matching to the InP layer. For the resonator modulator fabrication [see Fig. 1(e)], we designed a ring with an external radius of 42 µm and a Si ring width of 1.0 µm and 1.2 µm. See Section S1 of Supplement 1 for a detailed discussion about the design.

Figure 2 shows the details of the III-V epitaxial layer stack designed for the CRISP modulator. The quaternary composition of QW, QB, and SCH is chosen to maximize the EO effects in the modulator for operation at 4 K according to the following considerations: (i) the lattice constants match InP to avoid undesirable strain when the device is cooled down to 4 K; (ii) the exciton energy (i.e., photoluminescence) in the QWs is ~100 meV larger than the energy of the operating wavelength to prevent optical absorption ($\lambda \sim 1550$ nm corresponds to ~800 meV) [32]; and (iii) the energy gap and bandgap offset of QW and QB are designed to confine electrons and holes in the QW to maximize the QCSE as well as the band-filling and free-carrier dispersion effects [33,34]. By considering all these aspects, the alloy composition $In_xAl_{1-x-y}Ga_yAs$ used for QW, QB, and SCH are chosen to be ($x = 0.5296$, $y = 0.4512$), ($x = 0.5296$, $y = 0.3130$), and ($x = 0.5296$, $y = 0.3365$), respectively. See Section S2 of

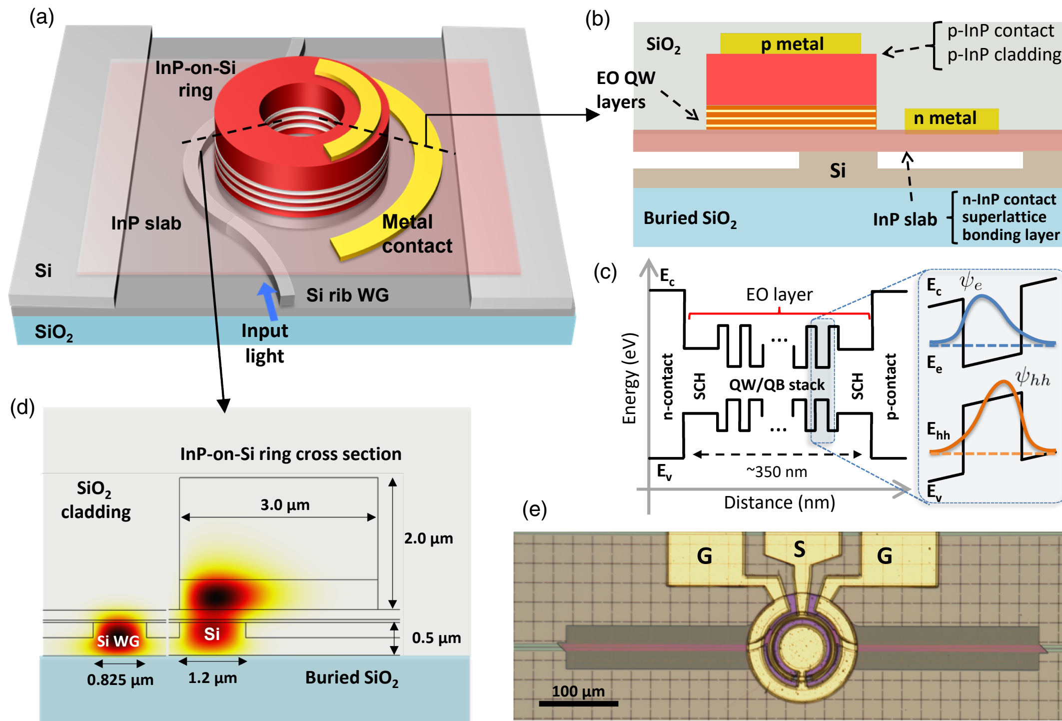

Fig. 1. Heterogeneously integrated InP-on-Si resonator modulator for operation at 4 K. (a) InP ring incorporating a stack of quantum wells bonded to a Si ring, forming an InP-on-Si ring resonator that is coupled to a Si waveguide. (b) Cross section of the stack of materials for the InP-on-Si modulator with metal contacts. (c) Energy bands of the electro-optic (EO) layer that contains a stack of quantum wells (QWs) and quantum barriers (QBs) in an alternating pattern, sandwiched between two separate confinement heterostructure (SCHs). The inset shows the wave functions of electrons (ψ_e) and heavy holes (ψ_{hh}) in the conduction and valence band, respectively. The conduction band energy level (E_c) and the valence band energy level (E_y) are shown with respect to their distances from the Si layer. The layer doping is optimized for large band-filling and plasma effects, while the QW geometry is engineered to maximize electron–hole interaction (excitons) to produce a strong quantum-confined Stark effect (QCSE). (d) Cross-section of optical mode profiles for the InP-on-Si resonator with a nominal external radius of 42 µm and for the Si waveguide, showing the mode overlap between the waveguide and the resonator modulator. (e) Optical microscope image of a fabricated ring modulator, showing metallic pads in ground–signal–ground (GSG) configuration for electric signals, and Si waveguide in a pulley coupling scheme with respect to the ring resonator.

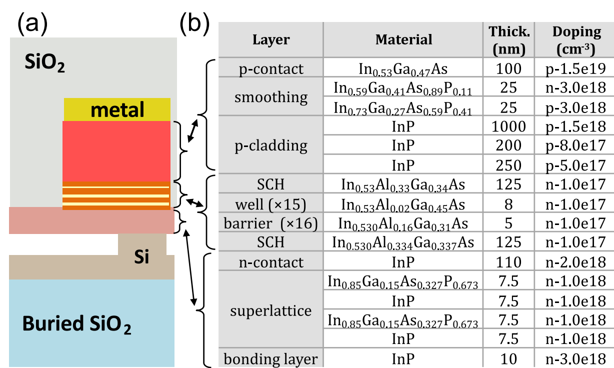

Layer	Material	Thick. (nm)	Doping (cm^{-3})
p-contact	$In_{0.53}Ga_{0.47}As$	100	p-1.5e19
smoothing	$In_{0.59}Ga_{0.41}As_{0.89}P_{0.11}$	25	n-3.0e18
	$In_{0.73}Ga_{0.27}As_{0.59}P_{0.41}$	25	p-3.0e18
p-cladding	InP	1000	p-1.5e18
	InP	200	p-8.0e17
	InP	250	p-5.0e17
SCH	$In_{0.53}Al_{0.33}Ga_{0.34}As$	125	n-1.0e17
well (×15)	$In_{0.53}Al_{0.02}Ga_{0.45}As$	8	n-1.0e17
barrier (×16)	$In_{0.530}Al_{0.16}Ga_{0.31}As$	5	n-1.0e17
SCH	$In_{0.530}Al_{0.334}Ga_{0.337}As$	125	n-1.0e17
n-contact	InP	110	n-2.0e18
superlattice	$In_{0.85}Ga_{0.15}As_{0.327}P_{0.673}$	7.5	n-1.0e18
	InP	7.5	n-1.0e18
	$In_{0.85}Ga_{0.15}As_{0.327}P_{0.673}$	7.5	n-1.0e18
	InP	7.5	n-1.0e18
bonding layer	InP	10	n-3.0e18

Fig. 2. III-V epitaxial layer designed and optimized for the 4 K operation of the CRISP modulator. (a) Schematic cross section of the CRISP ring resonator. (b) Epitaxial layers and their parameters.

Supplement 1 for more details on the material stack optimization. In addition, the three regions are lightly n-doped with a concentration of $\sim 1 \cdot 10^{17}/cm^3$ to obtain a larger change in the refractive index of $In_{1-x-y}Al_xGa_yAs$ through plasma and band-filling effects [35].

A microscope image of the final device is shown in Fig. 1(e), where the gold electrodes and the rib waveguide bus are identified. There is a 2 µm thick SiO_2 layer under the Si waveguides (buried oxide layer–BOX), and the samples are coated with a 1.5 µm thick SiO_2 cladding layer. See Section S3 of Supplement 1 for the details of the device fabrication process.

3. DEVICE CHARACTERIZATION

We characterize the EO performance of the CRISP modulator at a temperature of 4 K in a cryogenic probe station. We use lensed fibers to couple light into and out of the on-chip waveguides. The devices have a typical fiber-to-chip coupling loss of ~12 dB/facet. This excess loss can be reduced to a 2.5 dB/facet by optimizing the fabrication process [36]. See Section S9 of Supplement 1 for more details. At the output of the chip, we use optical and electronic amplifiers at room temperature to amplify the received signal for the measurement. See Sections S4–S6 of Supplement 1 for more details on the measurement.

Two key features of the resonator spectrum are needed to achieve a large optical modulation amplitude with a low driving voltage: (i) a large extinction ratio (ER) and (ii) a resonance with narrow FWHM. As shown in Fig. 3, the optical spectrum of the modulator has ER > 20 dB for λ near 1600 nm and for all applied voltage values between 0 V and −3.0 V. At this wavelength, the resonator has a loaded quality factor of ~53,000 corresponding to a FWHM of ~30 pm (~3.5 GHz). With such a slim resonance, a minimal applied voltage is sufficient to bring the ring out of the resonance while the large ER produces a high optical modulation

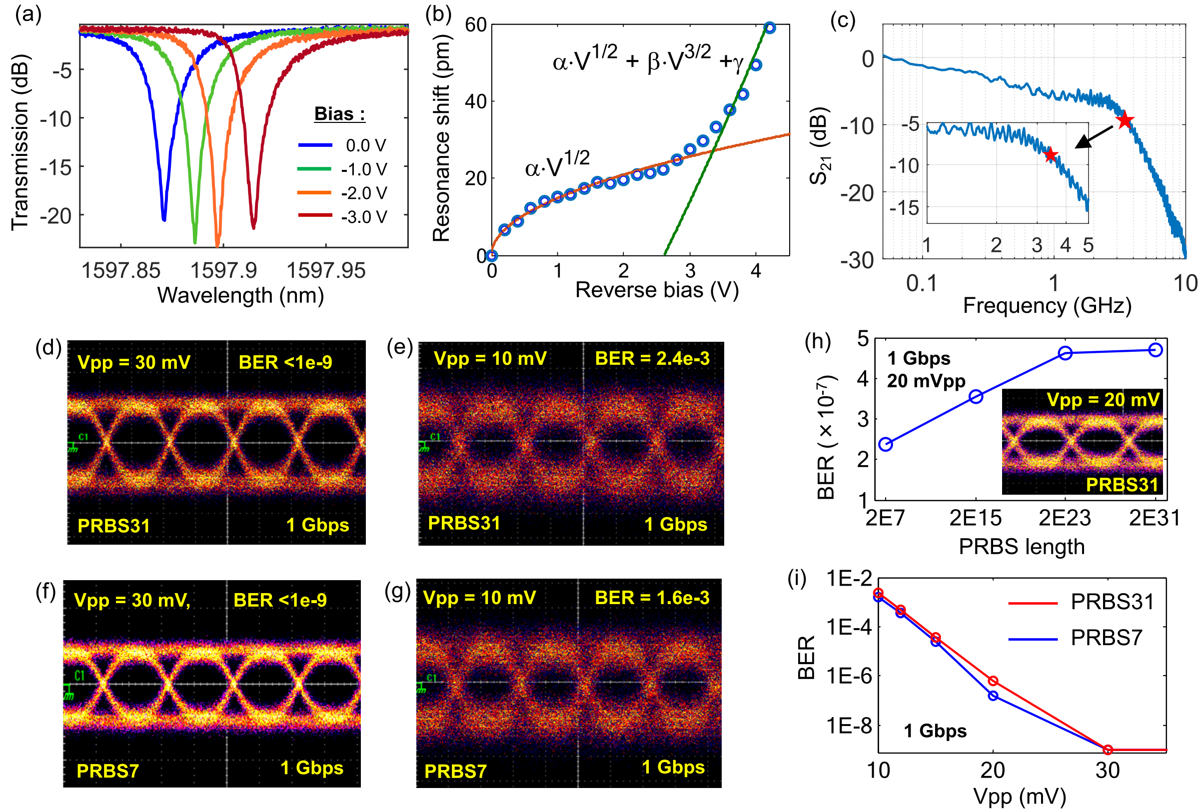

Fig. 3. CRISP modulator optimized for 10 mV scale operation at 4 K. (a) Spectrum of the resonator modulator at different reverse voltage bias values, with a FWHM for the resonance linewidth of ~30 pm. (b) Wavelength shift of the modulator resonance with respect to reverse bias voltage. The fits (lines) of measured data (circles) highlight the contributing modulation mechanisms. The resonance shift is proportional to $V^{1/2}$ for the band-filling and the plasma effects, while it varies as $V^{3/2}$ for the QCSE. The fitting parameters are the constants $\alpha = 14.79$ pm/$\sqrt{V}$, $\beta = 12.45$ pm/$\sqrt{V^3}$, and $\gamma = -76.36$ pm. (c) The electro-optical frequency response (S_{21} coefficient) of the modulator, with a pole at ~ 3.5 GHz that defines the bandwidth. (d)–(g) Demonstration of millivolt scale modulation at a 1 Gb/s data rate acquired by applying PRBS $2^{31}-1$ and PRBS 2^7-1 data streams to the modulator. For an input amplitude of 30 mV_{pp}, we achieve BER $<1e^{-9}$ limited by the noise floor of our BER equipment. The labels in (d)–(g) show the applied peak-to-peak modulation voltage (V_{pp}), bit error rate (BER), PRBS length, and the data rate. In (d) and (f), the electric energy consumption is 92 aJ/bit, and in (e) and (g) it is 10.4 aJ/bit. The modulator optical energy consumption in (d)–(g) is 213 fJ/bit. (h) BER versus PRBS length for a 1 Gb/s data rate and 20 mV_{pp} modulation amplitude. (i) The BER of the input signal decreases with an increasing modulation amplitude and the transmission is error free at 30 mV_{pp} and above. The modulator bias voltage for these experiments is −2 V and the on-chip optical power at the input of the modulator is 213 μW. The insertion loss of the chip is about 25 dB, mainly due to the fiber-to-chip coupling (~ 12 dB/facet).

amplitude. Since ER and FWHM depend on the ring-waveguide coupling coefficient [37], the modulator can be designed to operate at a different wavelength by optimizing the coupling coefficient at that wavelength.

The high sensitivity to electrical signals is shown in Fig. 3(b), where the resonance shift is plotted with respect to the applied reverse bias voltage. When the magnitude of the reverse bias is small, the spectrum shifts mainly because of the band-filling and the carrier depletion effects ($\Delta\lambda \propto V^{1/2}$). For much larger reverse bias voltages, the QCSE becomes the dominant contribution ($\Delta\lambda \propto V^{3/2}$). Taken together, these effects produce a nonuniform spectral shift with applied bias voltage [35]. From Fig. 3(b), we chose the optimal voltage bias point to provide large modulation sensitivity and minimum optical absorption. Although the resonance shift is much stronger in the QCSE regime, we bias the modulator where band-filling and plasma effects are dominant since we observed negligible absorption and no resonance linewidth broadening in this regime. An optimal future design can potentially bring down the absorption in the QCSE regime and thus allow its large resonance shift to be exploited.

Our modulator devices show a Gb/s modulation rate with a <10 mV_{pp} applied signal and ~10.4 aJ/bit electric energy consumption. We adjust the laser wavelength at the FWHM of the resonance, which has the maximum modulation sensitivity. The EO frequency response is shown in Fig. 3(c) and indicates a modulation bandwidth of around ~3.5 GHz. This value is limited by the optical resonance bandwidth of ~3.5 GHz due to the large loaded quality factor of the ring resonator ($Q \sim 53{,}000$). For the modulator data rate measurement, we apply pseudo-random bit sequences (PRBS) in the non-return-to-zero (NRZ) mode with lengths of $2^{31}-1$ and 2^7-1 and peak-to-peak voltage amplitude (V_{pp}) in the millivolt range. Figures 3(d)–3(g) show the measured eye diagrams for data rates of 1 Gb/s and different modulation amplitudes ranging down to 10 mV_{pp}. The total electric energy consumption per bit is given by $\frac{CV_{PP}^2}{4} + |V_{bias} I_{bias}|/r_b$, where C is the modulator capacitance, V_{bias} is the bias voltage, I_{bias} is the leakage current of the modulator, and r_b is the data rate. We measure a capacitance of $C \sim 406$ fF with a weak dependence on

bias voltage, as discussed in Section S6 of Supplement 1, resulting in $\frac{CV_{pp}^2}{4} \sim 10.1$ aJ/bit for $V_{pp} = 10$ mV. For this device, we observe a static leakage current of 0.14 nA, which corresponds to an energy consumption of 0.3 aJ/bit for a bias of −2 V and a data rate of 1 Gb/s. See Section S7 of Supplement 1 for more details. Therefore, we estimate the total electric energy consumption to be $E_b = 10.4$ aJ/bit. We believe that sub-aJ/bit electric energy consumption can be reached by reducing the electrode size and introducing an intrinsic region between the p and n doped areas, thus reducing the diode capacitance as well as the energy consumption [38]. Furthermore, we measured the bit error rate (BER) for each eye diagram shown in Figs. 3(d)–3(g). This metric quantifies the modulator performance for different input parameters such as bit sequence length, data rate, and modulation amplitude. We measure a BER $\sim 10^{-3}$ for $V_{pp} = 10$ mV, and a BER $< 10^{-9}$ for $V_{pp} = 30$ mV using PRBS with sequence lengths of both $2^{31}-1$ and 2^7-1 bits. Figure 3(h) shows the BER for various bit sequence lengths for 20 mV_{pp} of modulation amplitude, demonstrating similar BER (10^{-7}). Similarly, a plot of BER versus V_{pp} [Fig. 3(i)] shows the expected behavior of a decreasing BER with an increasing signal amplitude, and we observe error-free operation at amplitudes above 30 mV_{pp} for sequence lengths up to $2^{31}-1$ bits. With an on-chip optical input power of 213 µW, the optical energy consumption is 213 fJ/bit for these measurements. In our calculations, we have considered a more pessimistic case where all the on-chip optical power is lost in the resonator.

Figure 4 shows further experiments with the modulator device of Fig. 3, but for data rates up to 2 Gb/s and with 30 mV_{pp} modulation. We achieve error-free operation under these conditions using a PRBS with 2^7-1 bits. The BER versus V_{pp} curves clearly indicate an increase in BER with an increasing data rate [Fig. 4(c)]. Although this modulator has a bandwidth of ∼3.5 GHz, the limited bandwidth of our low-noise electronic amplifier (1.3 GHz), used to boost the room temperature photodetector signal, did not allow us to measure eye diagrams beyond 2 Gb/s for low modulation voltages.

A distinct advantage of the CRISP modulator is its lack of free carrier freeze-out, which leads to a wide modulation bandwidth at low temperatures. To verify this, we repeat the experiments with a second device that has a lower-Q resonator; hence, we get a larger resonance linewidth, and thereby a larger modulation bandwidth. We select a ring resonator with $Q \sim 20{,}000$ corresponding to a resonance linewidth of ∼80 pm [Fig. 5(a)]. Figure 5(b) shows the EO frequency response with a 3 dB bandwidth of ∼9 GHz, which is much wider than the results shown in Fig. 3(c). Note that we used a different electronic amplifier for this experiment (10 GHz bandwidth) after the photodetector.

Because of its larger resonance linewidth, this low-Q device requires a higher input voltage amplitude than the high-Q device to achieve a comparable optical modulation amplitude. Figures 5(c) and 5(d) show the measured eye diagrams at 4 Gb/s data rates for a modulation voltage of 110 mV_{pp}, and at different PRBS lengths (2^7-1 and $2^{15}-1$). The electrical energy consumption for this device is ∼1.3 fJ/bit, which is still small compared to prior demonstrations in the literature.

In a 4 K cryogenic system, the total energy consumption is dominated by that of the cryocooler, which scales with the power dissipation at the lowest temperature stage. For large-scale superconducting systems, where optical interconnects can offer a significant advantage, each watt dissipated at 4 K requires several hundred watts to be consumed by the cryogenic equipment [7]. Because of this steep penalty, dissipation by components located at the 4 K stage is the most critical metric to optimize, and power consumed by electrical and optical components at room temperature can be neglected.

Table 1 summarizes a comparison of the CRISP modulator with other demonstrated cryogenic EO modulators. As shown in the table, the CRISP modulator outperforms other EO modulators, operating at a significantly smaller driving voltage and with minimal electrical energy consumption. For all devices shown in Table 1, the optical energy consumption is comparable to or higher than the electrical one. Therefore, it is essential to reduce any optical dissipation and insertion loss. Table 1 excludes fiber-to-chip coupling loss, and only reports the inherent energy consumption of the modulator, which is the focus of this paper. Since fiber-to-chip coupling loss occurs inside the fridge, it can significantly impact the energy consumption budget at low temperatures. As the focus of this work is on inherent energy consumption of the modulator, a separate future work should address the optimization of the fiber-to-chip coupling with improved precision lithography and design strategy.

Since the CRISP modulator is resonator-based, tuning of the laser wavelength to the resonance wavelength is important for the optimal operation of the modulator. To reduce any energy load in the cryocooler, it is preferable to tune the wavelength of the laser that resides outside the fridge rather than tuning the resonator that is in the fridge. For a high throughput high data rate interconnect, we envision a bank of tunable lasers will be used at room temperature to drive a bank of modulators inside the fridge.

The radius of the CRISP resonators presented here is 42 µm, and it is possible to reduce this value in future devices. This will make the resonance shift more sensitive to low modulation voltage amplitudes, and it will also reduce the electrode capacitance, which increases the modulator bandwidth. However, proper designs of the InP and Si layer dimensions are required to prevent excessive bending loss when the resonator size is reduced. In this work, the highest intrinsic Q that we were able to achieve was ∼272,000, as discussed in Section S8 of Supplement 1. The large intrinsic Q of such resonator modulators can enable other applications, including sensing at cryogenic temperatures. This is a general advantage

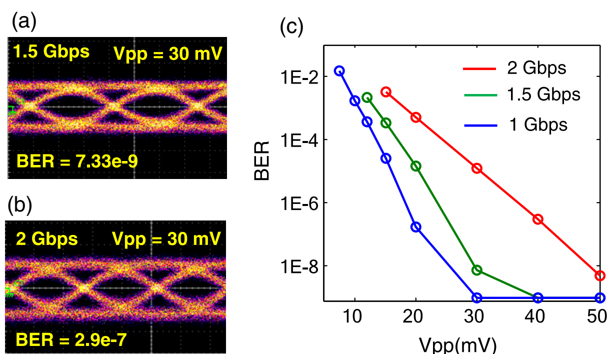

Fig. 4. Bit error rates for data rates up to 2 Gb/s at 4 K. A data rate of (a) 1.5 Gb/s and (b) 2 Gb/s, with a PRBS 2^7-1 pattern applied to the modulator device with characteristics shown in Fig. 3. The electrical energy consumption in both (a) and (b) is 92 aJ/bit, and the optical energy consumptions are 142 fJ/bit and 107 fJ/bit, respectively. (c) BER versus modulation voltage showing an increased error rate as the date rate goes up for a similar modulation voltage amplitude. The bias voltage and on-chip optical power are −2 V and 213 µW, respectively.

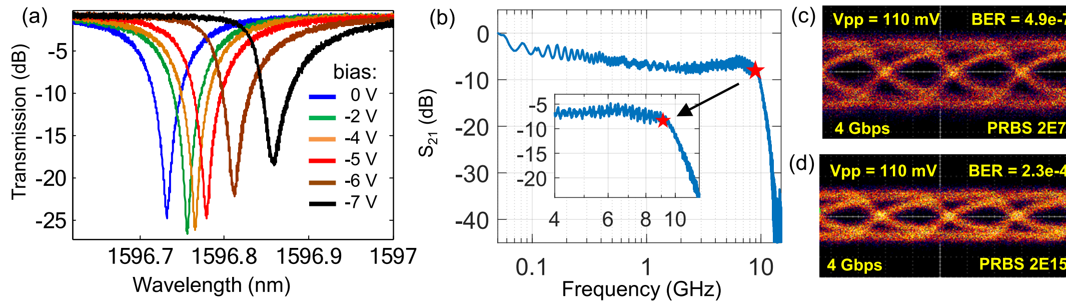

Fig. 5. CRISP modulators with a wider modulation bandwidth and higher data rates at 4 K. (a) Spectrum of a resonator modulator with a large resonance linewidth (∼80 pm) for multiple applied bias voltages levels. (b) The measured modulator frequency response has its lowest-frequency pole at ∼9 GHz, which sets the limit to the usable bandwidth. (c)–(d) The eye diagrams for data rates (modulation voltages) of 4 Gb/s ($V_{pp} = 110$ mV) for PRBS 2^7-1 and PRBS $2^{15}-1$, respectively. The modulator is biased at $V_{bias} = -6$ V ($I_{bias} = 0.08$ nA), operating predominantly in the QCSE regime. The eye diagrams and bandwidth are obtained for an on-chip optical power of 1.3 mW. The modulator electrical and optical energy consumption is 1.3 fJ/bit and 325 fJ/bit, respectively. The optical insertion loss of the chip is about 17 dB, mainly due to the fiber-to-chip coupling loss ∼8 dB/facet.

Table 1. Comparison of CRISP Modulator with Other Demonstrated Cryogenic EO Modulators

Material and Modulator Structure	BW (GHz)	Bit Rate (Gb/s)	Modulation Voltage (Vpp)	Electrical Energy	Optical Energy[c]	Ref.
LiNbO3 waveguide phase modulator	5	5	5 V	–	–	[14]
BaTiO3 microring, Pockels effect	30	20	1.7 V	45 fJ/bit	–	[13]
Graphene on SiN microring	14.7	20	3 V	20 fJ/bit	–	[18]
Si microdisk	4.5	10	1.8 V	80 fJ/bit	8 fJ/bit	[8]
Si MZI, DC Kerr	1.5	–	2 V	100 fJ/bit	–	[17]
Si ring	2.5	5	0.5 V	43 fJ/bit	–	[15]
Si ring	2.5	20	1.5 V	54 fJ/bit	–	[15]
Si microring with electric pre-amp	2.2	1	100 mV(4 mV)[a]	50 fJ/bit[b]	320 fJ/bit	[16]
Si microring with electric pre-amp	2.2	–	250 mV(10 mV)[a]	300 fJ/bit[b]	800 fJ/bit	[16]
InP-on-Si ring, QW Device #1 (Fig. 3)	4	1	10 mV	10 aJ/bit	213 fJ/bit	**This work**
InP-on-Si ring, QW Device #2 (Fig. 5)	9	4	110 mV	1.3 fJ/bit	275 fJ/bit	**This work**

[a]The numbers in parenthesis are the amplitudes applied to the pre-amplifier input. The amplifier gain is ∼28 dB.
[b]This is the power consumed by the cryogenic pre-amplifier that boosts the signal before it enters the modulator.
[c]This is the inherent optical energy consumption of the modulator, and it excludes the fiber-to-chip coupling loss.

compared to conventional Si modulators, where Q is limited to $\sim 10^4$ due to high doping-induced loss. Because of the high carrier mobility and lack of free carrier freezing in the InP layer of the CRISP architecture, the doping requirements are modest, which results in a low optical loss and high resonator Qs.

4. CONCLUSION

In summary, we have demonstrated a high-speed InP-on-Si electro-optic resonator modulator that operates at a temperature of 4 K with a record modulation voltage (∼10 mV_{pp}) performance and electric energy consumption (∼10.4 aJ/bit). We achieve these results by combining the EO properties of III-V-based QWs with the photonic integration capability of Si. The lack of free carrier freeze-out in InP and its compounds is a central feature since it enables efficient EO modulation with moderate doping, low loss, and a wide modulation bandwidth at cryogenic temperatures. With this active semiconductor platform, we achieve intrinsic Qs as high as 272,000 at 4 K, with much higher Q for larger radius resonators.

Although in this work, we demonstrate an individual resonator modulator device, the aggregate interconnect data bandwidth can be increased by integrating arrays of modulators with wavelength multiplexing. In the single-channel data links presented here, the external laser can be tuned to operate close to the ring resonance.

The demonstrated modulation voltage in this work is in the 10−30 mV_{pp} range, which is still large compared to SC digital logic circuits that have a voltage of a few millivolts. We believe the modulation voltage can be further reduced by optimizing the III-V epi structure of the CRISP modulator. It is also possible to boost the voltage using an all-superconducting amplifier [39] with a modest gain to amplify the SC signal before sending to the modulator. These modulators ultimately must be integrated with SC circuits. Interconnecting CRISP modulators and SC circuits can be accomplished using superconducting interposer modules. Recently, indium-based thermocompression flip-chip bonding has been used to couple SC circuitry with CMOS chips [40], and this technique also can be employed to interconnect PICs.

Our proposed solution paves the way for energy-efficient, high-bandwidth optical data links between cryogenic and room temperature environments. We believe this approach will resolve a critical bottleneck in the scaling of emerging cryogenic systems for classical and quantum information processing and sensing applications.

Funding. Army Research Office (W911NF-19-C-0060).

Acknowledgment. We greatly acknowledge the help and support from Mr. Richard Lazarus during the entire execution of the project. Any opinions, findings,

and conclusions or recommendations expressed in this material are those of the authors and do not necessarily reflect the views of the Army Research Office.

Disclosures. The authors declare no conflicts of interest.

Data availability. Data underlying the results presented in this paper are not publicly available at this time but may be obtained from the authors upon reasonable request.

Supplemental document. See Supplement 1 for supporting content.

†These authors contributed equally to the work.

REFERENCES

1. D. S. Holmes, A. L. Ripple, and M. A. Manheimer, "Energy-efficient superconducting computing—power budgets and requirements," IEEE Trans. Appl. Supercond. **23**, 1701610 (2013).
2. O. Mukhanov, A. Kirichenko, C. Howington, J. Walter, M. Hutchings, I. Vernik, D. Yohannes, K. Dodge, A. Ballard, B. L. T. Plourde, A. Opremcak, C.-H. Liu, and R. McDermott, "Scalable quantum computing infrastructure based on superconducting electronics," in *IEEE International Electron Devices Meeting (IEDM)* (2019), pp. 2019–2022.
3. K. Grutter, T. Salter, and T. Horton, "Findings of the 2nd Photonics and Electronics Technology for Extreme Scale Computing Workgroup (REPETE): Design challenges for socket level photonic I/O," arXiv:2110.11759 (2021).
4. F. Lecocq, F. Quinlan, K. Cicak, J. Aumentado, S. A. Diddams, and J. D. Teufel, "Control and readout of a superconducting qubit using a photonic link," Nature **591**, 575–579 (2021).
5. O. A. Mukhanov, D. Kirichenko, I. V. Vernik, T. Filippov, A. Kirichenko, R. Webber, V. Dotsenko, A. Talalaevskii, J. C. Tang, A. Sahu, P. Shevchenko, R. Miller, S. B. Kaplan, S. Sarwana, and D. Gupta, "Superconductor digital-RF receiver systems," IEICE Trans. Electron. **E91-C**, 306–317 (2008).
6. N. Ben Bekhti, A. Fröhlich, O. Grenz, F. König, L. Naumann, S. Putselyk, F. Rahlf, M. Tiesing, T. Wirths, and H. Wilden, "First studies towards a cryo-cooled phased array radar system for space surveillance," IOP Conf. Ser. Mater. Sci. Eng. **502**, 012194 (2019).
7. S. K. Tolpygo, "Superconductor digital electronics: scalability and energy efficiency issues," Low Temp. Phys. **42**, 361–379 (2016).
8. M. Gehl, C. Long, D. Trotter, A. Starbuck, A. Pomerene, J. B. Wright, S. Melgaard, J. Siirola, A. L. Lentine, and C. DeRose, "Operation of high-speed Si photonic micro-disk modulators at cryogenic temperatures," Optica **4**, 374–382 (2017).
9. S. Rumley, M. Bahadori, R. Polster, S. D. Hammond, D. M. Calhoun, K. Wen, A. Rodrigues, and K. Bergman, "Optical interconnects for extreme scale computing systems," Parallel Comput. **64**, 65–80 (2017).
10. O. A. Mukhanov, "Energy-efficient single flux quantum technology," IEEE Trans. Appl. Supercond. **21**, 760–769 (2011).
11. M. Tanaka, A. Kitayama, T. Koketsu, M. Ito, and A. Fujimaki, "Low-energy consumption RSFQ circuits driven by low voltages," IEEE Trans. Appl. Supercond. **23**, 0004301 (2013).
12. M. Tanaka, M. Ito, A. Kitayama, T. Kouketsu, and A. Fujimaki, "18-GHz, 4.0-aJ/bit operation of ultra-low-energy rapid single-flux-quantum shift registers," Jpn. J. Appl. Phys. **51**, 053102 (2012).
13. F. Eltes, G. E. Villarreal-Garcia, D. Caimi, H. Siegwart, A. A. Gentile, A. Hart, P. Stark, G. D. Marshall, M. G. Thompson, J. Barreto, J. Fompeyrine, and S. Abel, "An integrated optical modulator operating at cryogenic temperatures," Nat. Mater. **19**, 1164–1168 (2020).
14. A. Youssefi, A. Youssefi, I. Shomroni, Y. J. Joshi, N. R. Bernier, A. Lukashchuk, P. Uhrich, L. Qiu, and T. J. Kippenberg, "A cryogenic electro-optic interconnect for superconducting devices," Nat. Electron. **4**, 326–332 (2021).
15. H. Gevorgya, A. Khilo, D. Van Orden, D. Onural, B. Yin, M. T. Wade, V. M. Stojanović, and M. A. Popović, "Cryo-compatible, Si spoked-ring modulator in a 45 nm CMOS platform for 4K-to-room-temperature optical links," in *Optical Fiber Communication Conference (OFC)* (2021), paper M3B.3.
16. B. Yin, H. Gevorgyan, D. Onural, A. Khilo, M. A. Popović, and V. M. Stojanović, "Electronic-photonic cryogenic egress link," in *IEEE 47th European Solid State Circuits Conference (ESSCIRC)* (2021), pp. 51–54.
17. U. Chakraborty, J. Carolan, G. Clark, D. Bunandar, G. Glilbert, J. Notaros, M. R. Watts, and D. R. Englund, "Cryogenic operation of Si photonic modulators based on the DC Kerr effect," Optica **7**, 1385–1390 (2020).
18. B. S. Lee, B. Kim, A. P. Freitas, A. Mohanty, Y. Zhu, G. R. Bhatt, J. Hone, and M. Lipson, "High performance integrated graphene electro-optic modulator at cryogenic temperature," Nanophotonics **10**, 99–104 (2020).
19. X. Zhao and Z. Suo, "Electromechanical instability in semicrystalline polymers," Appl. Phys. Lett. **95**, 93–96 (2009).
20. Y. Xu, A. A. Sayem, C.-L. Zou, L. Fan, R. Cheng, and H. X. Tang, "Photorefraction-induced Bragg scattering in cryogenic lithium niobate ring resonators," Opt. Lett. **46**, 432–435 (2021).
21. S. M. Sze and K. K. Ng, *Physics of Semiconductor Devices* (John Wiley & Sons, 2006).
22. A. Melikyan, L. Alloatti, A. Muslija, D. Hillerkuss, P. C. Schindler, J. Li, R. Palmer, D. Korn, S. Muehlbrandt, D. Van Thourhout, B. Chen, R. Dinu, M. Sommer, C. Koos, M. Kohl, W. Freude, and J. Leuthold, "High-speed plasmonic phase modulators," Nat. Photonics **8**, 229–233 (2014).
23. W. Heni, Y. Fedoryshyn, B. Baeuerle, A. Josten, C. B. Hoessbacher, A. Messner, C. Haffner, T. Watanabe, Y. Salamin, U. Koch, D. L. Elder, L. R. Dalton, and J. Leuthold, "Plasmonic IQ modulators with attojoule per bit electrical energy consumption," Nat. Commun. **10**, 1–8 (2019).
24. T. Hiraki, T. Aihara, K. Hasebe, K. Takeda, T. Fujii, T. Kakitsuka, T. Tsuchizawa, H. Fukuda, and S. Matsuo, "Heterogeneously integrated III–V/Si MOS capacitor Mach–Zehnder modulator," Nat. Photonics **11**, 482–485 (2017).
25. J. H. Han, F. Boeuf, J. Fujikata, S. Takahashi, S. Takagi, and M. Takenaka, "Efficient low-loss InGaAsP/Si hybrid MOS optical modulator," Nat. Photonics **11**, 486–490 (2017).
26. T. Komljenovic, D. Huang, P. Pintus, M. A. Tran, M. L. Davenport, and J. E. Bowers, "Photonic integrated circuits using heterogeneous integration on Si," Proc. IEEE **106**, 2246–2257 (2018).
27. G. Roelkens, A. Abassi, P. Cardile, *et al.*, "III-V-on-Si photonic devices for optical communication and sensing," Photonics **2**, 969–1004 (2015).
28. B. R. Bennett, R. A. Soref, and J. A. Del Alamo, "Carrier-induced change in refractive index of InP, GaAs, and InGaAsP," IEEE J. Quantum Electron. **26**, 113–122 (1990).
29. S. L. Chuang, *Physics of Photonic Devices* (Wiley, 2009).
30. D. A. B. Miller, "Attojoule optoelectronics for low-energy information processing and communications," J. Lightwave Technol. **35**, 346–396 (2017).
31. A. Franciosi and C. G. Van De Walle, "Heterojunction band offset engineering," Surf. Sci. Rep. **25**, 1–140 (1996).
32. M. Guden and J. Piprek, "Material parameters of quaternary III–V semiconductors for multilayer mirrors at 1.55 μm wavelength," Model. Simul. Mater. Sci. Eng. **4**, 349–357 (1996).
33. H. Ohe, H. Shimizu, and Y. Nakano, "InGaAlAs multiple-quantum-well optical phase modulators based on carrier depletion," IEEE Photon. Technol. Lett. **19**, 1816–1818 (2007).
34. J. G. Mendoza-Alvarez, L. A. Coldren, A. Alping, R. H. Yan, T. Hausken, K. Lee, and K. Pedrotti, "Analysis of depletion edge translation lightwave modulators," J. Lightwave Technol. **6**, 793–808 (1988).
35. H.-W. Chen, *High-Speed Hybrid Si Mach-Zehnder Modulator and Tunable Microwave Filter* (University of California, 2011).
36. R. Marchetti, C. Lacava, L. Carroll, K. Gradkowski, and P. Minzioni, "Coupling strategies for Si photonics integrated chips [invited]," Photon. Res. **7**, 201–239 (2019).
37. W. Bogaerts, P. De Heyn, T. Van Vaerenbergh, K. De Vos, S. K. Selvaraja, T. Claes, P. Dumon, P. Bienstman, D. Van Thourhout, and R. Baets, "Si microring resonators," Laser Photon. Rev. **6**, 47–73 (2012).
38. G. L. Li and P. K. L. Yu, "Optical intensity modulators for digital and analog applications," J. Lightwave Technol. **21**, 2010–2030 (2003).
39. M. H. Nguyen, G. J. Ribeill, M. V. Gustafsson, *et al.*, "Cryogenic memory architecture integrating spin Hall effect based magnetic memory and superconductive cryotron devices," Sci. Rep. **10**, 248 (2020).
40. R. N. Das, V. Bolkhovsky, S. K. Tolpygo, P. Gouker, L. M. Johnson, E. A. Dauler, and M. A. Gouker, "Large scale cryogenic integration approach for superconducting high-performance computing," in *IEEE 67th Electronic Components and Technology Conference (ECTC)* (2017), pp. 675–683.

210.28.142.31 {ts '2022-10-20 23:40:01'}